# Parametric Raman Wavelength Conversion in Scaled Silicon Waveguides

Varun Raghunathan, Ricardo Claps, Dimitrios Dimitropoulos, and Bahram Jalali, *Fellow, IEEE*

***Abstract*—The benefits of using submicrometer modal-dimension silicon waveguides in realizing high-efficiency parametric Raman wavelength conversion are demonstrated theoretically and experimentally. The combined effects of Raman nonlinearities and free-carrier losses induced by two-photon absorption (TPA) are analyzed using the coupled-mode theory. The analysis indicates that scaling down the lateral dimensions increases the conversion efficiency of the Raman process and reduces the effective lifetime of free carriers and hence ameliorates the free-carrier losses. The feasibility of data conversion is demonstrated by coherent transfer of the analog radio-frequency (RF) signal from Stokes to anti-Stokes channels. The conversion efficiency, and hence signal-to-noise ratio (SNR), and bandwidth of the conversion process are found to be limited by the phase mismatch between the pump, Stokes, and anti-Stokes fields. The dispersion properties of submicrometer waveguides are also studied from the point of view of achieving phase matching and enhancing the conversion efficiency.**

***Index Terms*—Integrated optics, nonlinear optics, Raman scattering, silicon-on-insulator (SOI), wavelength conversion.**

## I. Introduction

SILICON has many desirable physical and economical properties that render it a potential platform for optical and optoelectronic integration [1]. On the economics side, the quality of commercial silicon wafers continues to improve while the wafer cost continues to decrease. At the same time, nanoscale device fabrication has entered volume manufacturing, keeping alive the trend toward lower cost and higher performance. Silicon photonics can, optimistically, be perceived as an extension of silicon complementary metal–oxide–semiconductor (CMOS) technology that can meet the increasing demands for faster interconnects on chip and between chips. Despite success in making high-quality passive devices [2], silicon photonics has been hindered by the lack of suitable active functionality. Recently, good progress has been made in realizing active functionalities. This includes light generation and amplification in silicon nanocrystals [3], [7], $Er^{3+}$-doped silicon waveguide structures [4] and $Er^{3+}$-doped silicon nanocrystals [5], [6]. Optical modulation using metal–oxide–semiconductor (MOS) capacitance [8] and free-carrier dispersion effects [9] and photodetection using silicon–germanium heterostructures [10].

Another approach toward realizing active functionalities is to make use of the nonlinear optical properties of silicon. The silicon-on-insulator (SOI) platform is best suited for nonlinear optics, because of the high-index contrast between silicon and silica ($\Delta n \sim 2$), which results in the strong optical confinement needed to observe optical nonlinearities. Recently, there has been substantial interest in this direction with the demonstration of Raman amplification in continuous-wave [11]–[13] and pulsed [14], [15] pumping conditions, anti-Stokes Raman conversion [16], [17], supercontinuum generation [18], cross-phase modulation [19], two-photon absorption (TPA) [20] and four-wave mixing (FWM) [21].

This paper presents the theoretical and experimental results demonstrating wavelength conversion using parametric Raman nonlinearities in submicrometer modal-dimension silicon waveguides. The interplay between the Raman conversion process and TPA-induced free-carrier losses are studied using the coupled-mode theory formalism. The analysis indicates that scaling down the waveguide dimensions increases the conversion efficiency of the Raman process and reduces the effective lifetime of free carriers, thereby suppressing the free-carrier losses. The dispersion properties of these scaled waveguides are also studied from the point of view of reducing phase mismatch and enhancing the conversion efficiency.

## II. Theory

### A. Parametric Raman Conversion

Stimulated Raman scattering involves the simultaneous generation of Stokes and anti-Stokes fields with the Stokes field experiencing amplification and exponential growth with length. However, the extent to which the above assertion is true depends on the phase mismatch between the pump ($k_P$), Stokes ($k_S$), and anti-Stokes ($k_A$) fields, which is given as $\Delta k = 2k_p - k_S - k_A$. As $\Delta k$ tends to zero, the three fields experience parametric coupling. This leads to exchange of information between the Stokes and anti-Stokes channels. The Raman amplification process is suppressed, and the Stokes/anti-Stokes fields grow linearly with length. The vibrational energy levels of silicon and the parametric Raman interaction are shown in Fig. 1. Close to $\Delta k = 0$, the two processes shown in Fig. 1 strongly couple through the mediation of coherently generated phonons leading to coherent transfer of information between the Stokes and anti-Stokes fields.

Manuscript received September 20, 2004; revised February 28, 2005. This work was supported by the MTO office of the Defense Advance Research Project Agency (DARPA).

V. Raghunathan, D. Dimitropoulos, and B. Jalali are with the Department of Electrical Engineering, University of California, Los Angeles (UCLA), Los Angeles, CA 90095-1594 USA.

R. Claps was with the Department of Electrical Engineering, University of California, Los Angeles (UCLA), Los Angeles, CA 90095-1594 USA. He is now with Neptec Optical Solutions, Inc., Jefferson City, TN 37760 USA.

Digital Object Identifier 10.1109/JLT.2005.849895

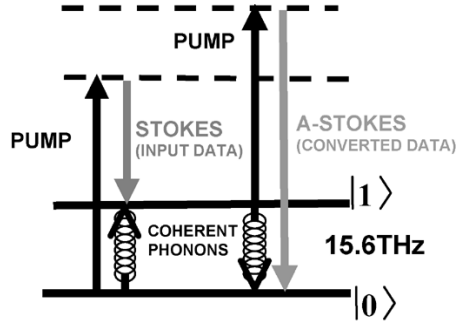


Fig. 1. Vibrational energy levels of silicon and the Raman wavelength conversion process. Modulated data in the Stokes input signal is coherently converted to the anti-Stokes signal through the mediation of coherent optical phonons.

In this regime, the Raman nonlinearities can be used to perform wavelength conversion across widely spaced channels (2 × Raman shift = 31.2 THz in silicon i.e., >200 nm for telecom wavelengths). One of the applications of the Raman wavelength converter in silicon is as a chip–scale interface between present-day optical networks, which efficiently operate at 1550-nm band and silicon–germanium detectors, which exhibit efficient response in the 1300-nm band. In silicon, this process is more efficient than electronic susceptibility-based FWM because the Raman susceptibility ($\chi_R^{(3)} = 11.2 \times 10^{-14}$ cm$^2$/V$^2$) [22] is ∼44 times larger than the electronic one ($\chi_E^{(3)} = 0.25 \times 10^{-14}$ cm$^2$/ V$^2$) [23]. However, the Raman process being resonant has a characteristic Lorenztian gain profile (bandwidth ∼105 GHz in silicon), which determines the response of the conversion process to wavelength detuning from the peak.

### *B. Two-Photon and Free-Carrier Absorption*

TPA is another nonlinear optical process that occurs at high pump intensities and could compete with the Raman nonlinearities. It has been experimentally found that the depletion of the pump due to TPA is negligible at typical continuous-wave (CW) pump powers used to observe Raman nonlinearities [11]. However, the free carriers generated during this TPA process lead to nonlinear absorption losses that could reduce the observed Raman nonlinearities. The energy levels of silicon and theTPA and free-carrier absorption (FCA) are shown in Fig. 2.

This FCA process has been identified as a limit in all-optical switching in III–V semiconductor waveguides [24] and has also been studied in silicon waveguides [12]. The TPA-induced free-carrier loss is described by the Drude model [25] as

$$\Delta\alpha_{\mathrm{FCA}} \cong 6.04 \times 10^{-18}\lambda^2\,(\mu\mathrm{m}) \cdot \frac{\beta I_p^2 \tau_{\mathrm{eff}}}{2E_p}. \tag{1}$$

Here, $\beta$ is the TPA coefficient (= $5 \times 10^{-10}$ cm/W for silicon), $\lambda$ is the pump wavelength, $\tau_{\mathrm{eff}}$ is the effective carrier lifetime, and $E_p$ is the photon energy.

The carrier lifetime in SOI samples depend on the method used for fabrication of the wafer and the film thickness, with reported values ranging between 10 and 200 ns [26]. The lifetime is primarily limited by the interface recombination at the

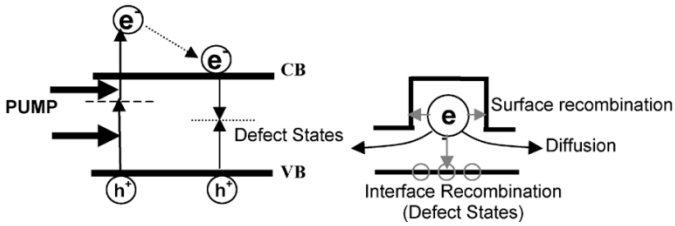


Fig. 2. Electronic energy levels of silicon and the TPA process. Free carriers generated during this process increase the overall loss. The carriers are depleted by interface and surface defect state recombination and transit out of the optical mode region in the rib structure.

silicon and buried oxide interface and surface recombination at the waveguide sidewalls (Fig. 2). In rib waveguides, the lifetime is further reduced by lateral diffusion of carriers away from the optically active waveguide core (Fig. 2). In rib-waveguide structures with width $w$, rib height $H$, and slab height $h$, the effective lifetime can be written as [27]

$$\frac{1}{\tau_{\mathrm{eff}}} = \frac{1}{\tau} + \frac{S}{H} + \frac{w + 2(H-h)}{wH} S' + 2\frac{h}{H}\sqrt{\frac{D}{w^2}\left(\frac{1}{\tau} + \frac{S+S'}{h}\right)}. \tag{2}$$

Here, $\tau$ refers to the bulk recombination lifetime (hundreds of microseconds in bulk silicon). The other three terms refer to the interface recombination lifetime, surface recombination at the sidewalls, and transit time out of the modal area, respectively. $S = 4 \times 10^3$ cm/s, $S'$ could range from 10 cm/s to $10^4$ cm/s, depending on the quality of the sidewalls, and $D = 16$ cm$^2$/s are the effective surface recombination velocity and ambipolar diffusion coefficient, respectively [27]. The bulk recombination lifetime is much larger than the other two contributions. Hence, the effective lifetime is determined by the dimensions $H$, $w$, and $h$, and the ratio $r = h/H$. Thus, (2) shows that $\tau_{\mathrm{eff}}$ reduces with scaling down of the rib dimensions, and this in turn reduces the FCA losses. The reduction in FCA losses with reducing dimensions holds true for constant pump intensities. However, as the carrier lifetimes are reduced to 1 ns and lower FCA losses reach negligible levels, Raman nonlinearities dominate over FCA effects, even with increasing pump intensities. This is further explained in Section II-D.

### *C. Coupled-Mode Analysis*

The evolution of the pump $P$, Stokes $S$, and anti-Stokes $A$ fields along the length of the waveguide can be described by the coupled-mode equations as (assuming $|E_P| > |E_S| > |E_A|$) [22], [28]

$$\begin{aligned}
\frac{dE_P}{dz} &= -\frac{(\alpha + \Delta\alpha_{\mathrm{FCA}-P}(z))}{2}E_P - \frac{\beta}{2}|E_P|^2 E_P \\
\frac{dE_S}{dz} &= -\frac{(\alpha + \Delta\alpha_{\mathrm{FCA}-S}(z))}{2}E_S + \kappa_{SS}E_S \\
&\quad + \kappa_{SA}E_A^*.\exp(-i\Delta kz) \\
\frac{dE_A^*}{dz} &= -\frac{(\alpha + \Delta\alpha_{\mathrm{FCA}-AS}(z))}{2}E_A^* + \kappa_{AA}E_A^* \\
&\quad + \kappa_{AS}E_S.\exp(+i\Delta kz)
\end{aligned} \tag{3}$$

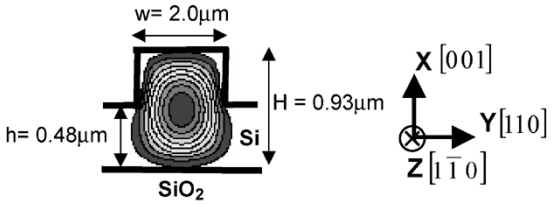


Fig. 3. Cross-sectional profile of the waveguide and the transverse-electric (TE) mode coupled into the waveguide. The dimensions of the waveguide are width $w = 2\ \mu$m, rib height $H = 0.93\ \mu$m, and slab height $h = 0.48\ \mu$m. Also shown is the crystallographic orientation of the SOI waveguides.

where $\kappa$'s refer to the coupling coefficients, which are given as

$$\kappa_{SS} = -i \cdot \left( \frac{2\pi\omega_S^2}{c^2 k_S} \left( 2\chi_E^{(3)} + \chi_R^{(3)}(\Omega) \right) - i\beta \right) |E_P|^2$$
$$\kappa_{SA} = -i \cdot \frac{2\pi\omega_S^2}{c^2 k_S} \left( \chi_E^{(3)} + \chi_R^{(3)}(\Omega) \right) E_P^2$$
$$\kappa_{AA} = +i \cdot \left( \frac{2\pi\omega_A^2}{c^2 k_A} \left( 2\chi_E^{(3)} + \chi_R^{(3)}(-\Omega) \right) - i\beta \right)^* |E_P|^2$$
$$\kappa_{AS} = +i \cdot \frac{2\pi\omega_A^2}{c^2 k_A} \left( \chi_E^{(3)} + \chi_R^{(3)}(-\Omega) \right)^* E_P^{*\,2}. \quad (4)$$

$\alpha$ refers to the linear absorption loss, which is assumed to be the same for the three fields. However, since the three fields span $\sim$200 nm in wavelength, the linear losses could be different at these wavelengths. $\Delta\alpha_{\mathrm{FCA}}$ refers to the FCA losses as given by (1). Depletion of the pump, Stokes, and anti-Stokes by the TPA process has also been included. The phase mismatch $\Delta k$ determines the extent of coupling between the Stokes and anti-Stokes fields. With the assumption $(\omega_P^2/k_P) \approx (\omega_S^2/k_S) \approx (\omega_A^2/k_A) = (\omega^2/k)$, the Raman gain coefficient is written as $G = (-i\chi_R^{(3)}(\Omega)4\pi\omega^2)/(c^2 k) = 2.0 \times 10^{-8}$ cm/W [11], and the contribution to the electronic nonlinearity is written as $R = (\chi_E^{(3)} 2\pi\omega^2)/(c^2 k) = 1.7 \times 10^{-9}$ cm/W [16]. The cross section of the SOI waveguide and its crystallographic orientation is shown in Fig. 3. The dependence of the conversion efficiency on the crystallographic axes can be described based on the selection rules obtained using the Raman tensors [29]. Moreover, the relative polarization of the pump and signal with respect to the crystallographic axes determines the contribution of birefringence to phase mismatch and hence the conversion efficiency. This is further discussed in Section IV.

### *D. Theoretical Results and Discussions*

The coupled-mode equations presented previously were solved numerically. Conversion is assumed to occur from a Stokes to an anti-Stokes wavelength with no initial anti-Stokes signal. The conversion efficiency of the wavelength conversion process across a waveguide of length $L$ is defined as $\eta = P_A(L)/P_S(0)$, with $P \propto |E|^2$. This theoretical analysis also holds true for anti-Stokes-to-Stokes conversion, but the conversion efficiency differs by the factor $(\kappa_{SA}/\kappa_{AS})^2$. The waveguides used in the experiments were simulated using the beam-propagation method (BPM), and the modal profile is shown in Fig. 3. From this, the modal area was extracted to be 0.54 $\mu$m$^2$. In all the theoretical results discussed here, uniform linear propagation losses of $\alpha = 1$ dB/cm and a waveguide length of $L = 2.5$ cm has been assumed, unless stated otherwise.

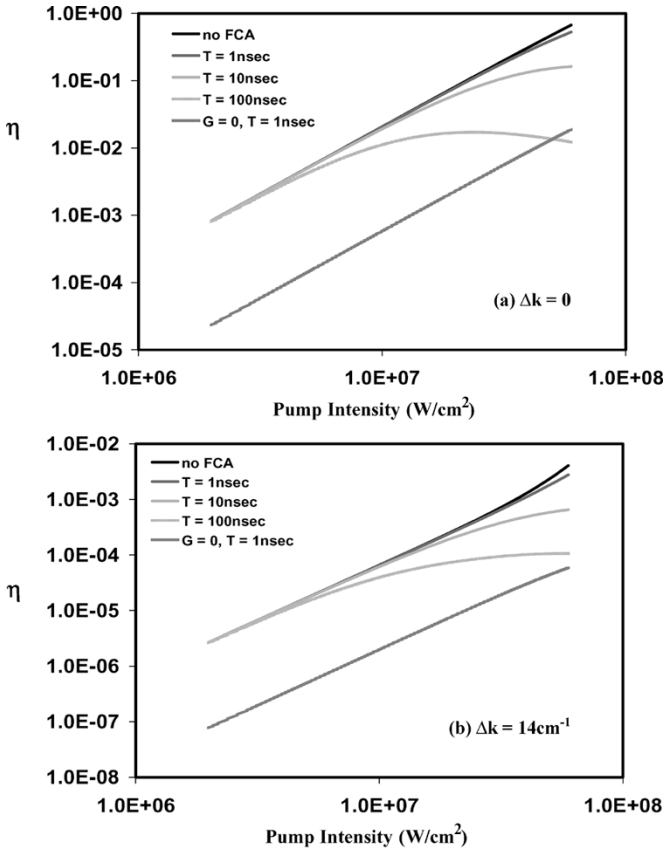


Fig. 4. Variation of conversion efficiency with pump intensity for (a) phase-matched condition $\Delta k = 0$ and (b) with phase mismatch $\Delta k = 14\ \mathrm{cm}^{-1}$. The plots are shown for carrier lifetimes of 1, 10, and 100 ns and no FCA effects. Also shown are the curves with no Raman susceptibility involved $(G = 0)$, where only electronic nonlinearity is present.

The variation of conversion efficiency with pump intensity is shown in Fig. 4 for the phase-matched case [Fig. 4(a)] and for a phase mismatch of 14 cm$^{-1}$ [Fig. 4(b)]. The conversion is most efficient at the phase-matched condition, and in this case, with no FCA losses, the conversion efficiency varies quadratically with pump intensity [28]. For nonzero $\Delta k$, the variation is more complex with pump intensity. The saturation of efficiency for increasing carrier lifetimes is due to the TPA-induced FCA losses. FCA effects are a concern for carrier lifetimes of larger than 10 ns. For a lifetime of 1 ns and lower, the curves essentially follow the case with no free-carrier losses, and hence free-carrier losses are negligible. Thus, scaling down of waveguide dimensions to achieve lifetimes of $<$1 ns offers a twofold advantage in enhancing the Raman nonlinearities due to an increase in optical intensities coupled into the waveguide and reducing FCA effects to negligible levels.

Conversion efficiency is also shown for the case in which only electronic nonlinearities contribute to conversion $(G = 0)$. Even with negligible FCA losses $(\tau_{\mathrm{eff}} = 1\ \mathrm{ns})$, the efficiency is $\sim$18 dB less than the Raman conversion case. This is because of the weaker electronic susceptibility when compared with the Raman contribution as discussed previously.

The $\mathrm{Sinc}^2$ dependence of conversion efficiency on phase mismatch at a fixed pump intensity of $6 \times 10^7$ W/cm$^2$ is shown in

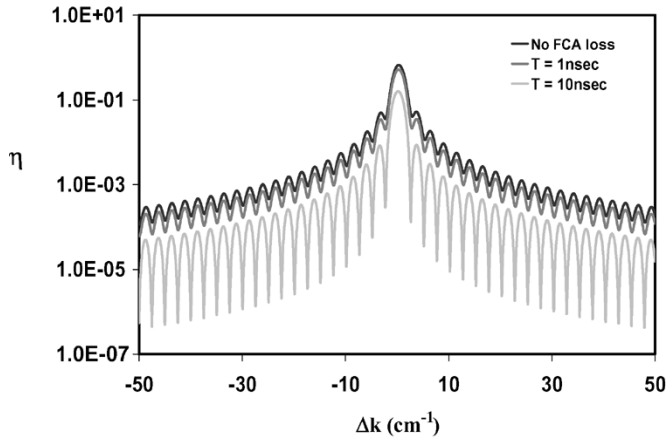


Fig. 5. Dependence of conversion efficiency on phase mismatch is shown for various carrier lifetimes and also for the case with no FCA effects.

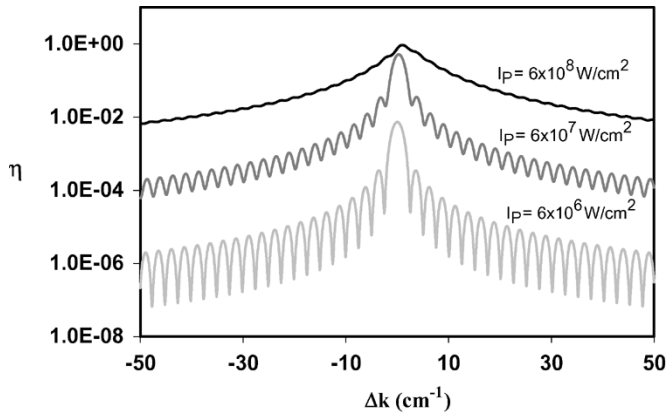


Fig. 6. Dependence of conversion efficiency on phase mismatch is shown for various pump intensities. The amplitude of the ripples reduces with increasing intensity, and the shift of maximum efficiency to $\Delta k > 0$ is due to modulation instability effects.

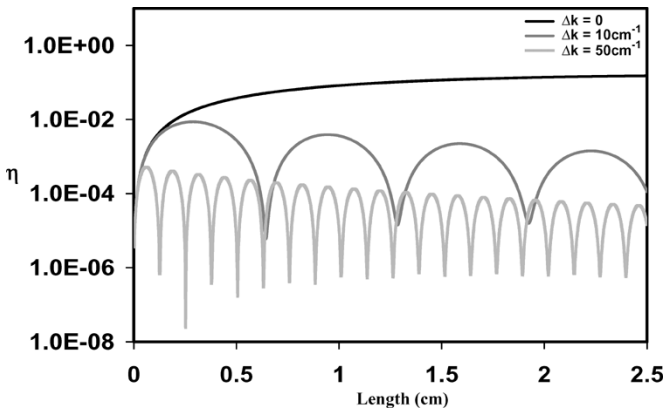


Fig. 7. Evolution of conversion efficiency along the propagation direction for phase-matched case and phase mismatch of 10 and 50 $\text{cm}^{-1}$ are shown for carrier lifetime of 1 ns. At phase mismatch, the ripples are due to the periodic reversal of phase between the various field.

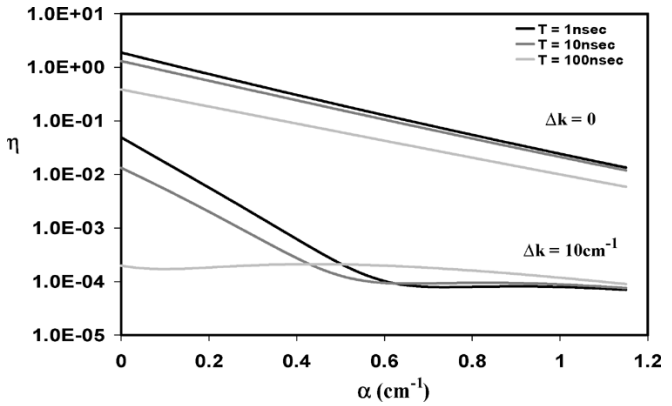


Fig. 8. Dependence of conversion efficiency on linear propagation losses are shown for phase-matched case and a phase mismatch of 10 $\text{cm}^{-1}$. Also shown are the plots for carrier lifetimes of 1, 10, and 100 ns. For losses less than 0.55 $\text{cm}^{-1}$ or 2.5 dB/cm, the FCA losses dominate and determine the conversion efficiency. However, for losses larger than 2.5 dB/cm, FCA effects are minimal, but overall conversion efficiency is less due to high linear loss in this regime.

Fig. 5. The efficiency is strongly dependent on $\Delta k$ with a reduction of more than 20 dB for $\Delta k \sim 10$ $\text{cm}^{-1}$. This emphasizes the importance of achieving phase matching in order to enhance the conversion efficiency. Also shown in Fig. 5 are the curves for various carrier lifetimes. As the efficiency reduces with increasing carrier lifetimes, the amplitude of the ripples is found to increase. Many values of phase mismatch can achieve the same conversion efficiency, and the range of $\Delta k$, which achieves a given conversion efficiency, increases for larger values of phase mismatch. In general, the oscillatory dependence on $\Delta k$ implies that phase mismatch must be accurately engineered to achieve a given efficiency.

Fig. 6 shows the efficiency versus $\Delta k$ for varying pump intensities. A carrier lifetime of 1 ns has been assumed. With increasing pump intensity, the conversion efficiency increases as expected, and the $\text{Sinc}^2$ curve approaches a monotonically decreasing function of $\Delta k$. This implies that at higher intensities, the conversion efficiency is less sensitive to small variations in $\Delta k$. Higher intensities result from high pump powers or smaller waveguide cross sections. The latter is preferred for multiple reasons as it also reduces free-carrier accumulation, as discussed previously. The slight shift in the peak conversion efficiency to $\Delta k > 0$ is due to modulation instability effects that occur at $\partial^2 k/\partial\omega^2 < 0$ [30].

The evolution of conversion efficiency along the propagation length is shown in Fig. 7 for a fixed pump intensity of $6\times10^7$ $\text{W/cm}^2$. The oscillatory nature of the curves for nonzero $\Delta k$ is a manifestation of the periodic reversal in the phase relationships and, hence, the parametric conversion process as determined by the coherence length [30]. The combined contributions of the linear propagation losses and the free-carrier losses lead to the decrease in conversion efficiency with length. Although it is beneficial under phase mismatch to use shorter length waveguides to achieve higher conversion efficiencies, the amplitude of the ripples also increases for shorter lengths, necessitating a more precise control of waveguide length.

Next, we show the dependence of conversion efficiency on the linear propagation loss for various carrier lifetimes and $\Delta k = 0$ and 10 $\text{cm}^{-1}$ (Fig. 8). A constant pump intensity of $6 \times 10^7$ $\text{W/cm}^2$ has been assumed. We obtain two different regimes, depending on the relative contribution of FCA loss to the overall loss in the waveguide. As the linear propagation loss increases and contributes significantly to the overall loss in the waveguide,

the effect of FCA loss on the conversion process becomes negligible. The linear propagation loss at which this happens depends on the waveguide length and pump intensity achieved in the waveguide. Under the given conditions, for linear loss of less than 0.55 $cm^{-1}$ ($\sim$2.5 dB/cm), FCA loss dominates. This is seen from the different profiles for the curves corresponding to various lifetimes. For losses larger than 2.5 dB/cm, the linear loss dominates, and the curves for different lifetimes follow a similar trend. However, as the linear propagation loss increases, the conversion efficiency is also reduced significantly.

From this analysis, it is found that scaling down the waveguide dimensions to submicrometer dimensions and low propagation losses enhances the Raman nonlinearities and reduces carrier lifetime and, hence, free-carrier effects. An increase in pump intensity not only enhances Raman nonlinearities, but also relieves the stringent requirements on phase mismatch to achieve high conversion efficiency. Engineering $\Delta k$ close to zero would further help in enhancing the conversion efficiency. Experimental results on scaled silicon waveguides are presented in Section III. The various contributions to phase mismatching and the different means to achieve phase matching are presented in the Section IV.

## III. Experimental Results

The experimental setup used for wavelength conversion as shown in Fig. 9 consists of a CW pump at 1427.3 nm (TE polarized) and an external-cavity diode laser (ECDL) used as the Stokes source at 1542.3 nm (TE polarized). The ECDL is amplified before combining with the pump. At the output end, a bandpass filter is used to extract the converted anti-Stokes signal at 1328.8 nm (TE polarized) before observing the converted power using an optical spectrum analyzer (OSA) or radio-frequency spectrum analyzer (RFSA). The SOI rib waveguide used is 2.5 cm long with dimensions as shown in Fig. 3 and a modal area of $\sim$ 0.54 $\mu m^2$. The propagation losses in these waveguides at 1328.8 nm were estimated to be $\sim$2.5 dB/cm using the Fabry–Pérot resonance technique. The polarization configuration used in this paper is different from our previous report [16], [17]. The reason for this is the different dispersion properties of the submicrometer modal-dimension waveguides as discussed in Section IV.

Total anti-Stokes-converted power of 2.3 nW is measured (see inset of Fig. 10) at 1.8 mW of Stokes input power and 0.23 W of pump. Taking into account the coupling losses, the net conversion efficiency is found to be $1.7\times10^{-5}$. The input Stokes wavelength was tuned from 1535 to 1550 nm, and the conversion efficiency between the input (Stokes) and the converted output (anti-Stokes) as obtained using the optical spectrum analyzer is shown in Fig. 10. A clear peak is obtained at the Raman resonance, and the "satellite" peaks are a manifestation of the $\mathrm{Sinc}^2$ functional dependence of conversion efficiency on phase mismatch, which in turn depends on the wavelength. The bandwidth of the conversion process is determined by the Raman gain profile and the pump laser linewidth. It can be increased by using many pump lasers or a broader linewidth pump laser. However, the use of a broader pump would reduce the magnitude of the Raman nonlinearities [11].

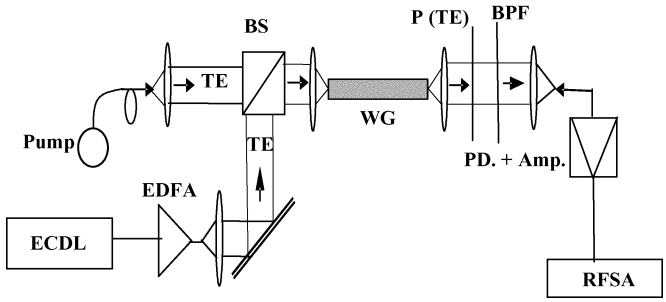


Fig. 9. Experimental setup for wavelength conversion, pump: pump laser at 1427.3 nm. ECDL: External-cavity diode laser at 1542.3 nm (Stokes); MOD.: modulator; BS: beam splitter; WG: waveguide; P (TE): polarizer to collect TE0 mode; BPF: bandpass filter at 1328.8 nm (anti-Stokes); PD.+Amp.: photodetector and amplifier; RFSA: radio-frequency (RF) spectrum analyzer.

A figure of merit that characterizes the improvement in the conversion process as the waveguide cross section is scaled down is $F = \eta/P_P$. For the submicrometer modal-dimension waveguides used in this paper, $F = 7.4 \times 10^{-5}$ $W^{-1}$, while in our previous report on micrometer-sized waveguides, $F = 1.4 \times 10^{-5}$ $W^{-1}$ [16], [17]. This improvement by more than a factor of five can be attributed to the increased Raman nonlinearities and the reduced carrier lifetime due to submicrometer modal-dimension waveguides.

The dependence of conversion efficiency on pump intensity is shown in Fig. 11(a). Theoretical fit (solid line) to the experimental data using the analysis of Section II shows good agreement for an effective lifetime of 10 ns and $\Delta k$ in the range of 15–120 $cm^{-1}$. The $\mathrm{Sinc}^2$ dependence of efficiency on phase mismatch leads to multiple values of $\Delta k$, satisfying the obtained efficiency. This prevents us from extracting the exact value of $\Delta k$ using this method. Using (2), the effective carrier lifetime can be extracted to be $>$5 ns, depending on the surface recombination velocity. This is in reasonable agreement with the above fit. When the pump and Stokes signals are cross-polarized, the conversion is found to be less efficient as shown in curve b in Fig. 11. This is because of the larger phase mismatch when compared with the parallel-polarized case, as will be discussed in the next section.

The conversion of analog radio-frequency (RF) modulation from Stokes to anti-Stokes channels is shown in Fig. 12. An RF signal at 1.03 GHz was modulated at the Stokes wavelength and converted to the anti-Stokes wavelength. The converted anti-Stokes signal was detected and amplified before observing the modulation using an RF spectrum analyzer. The output shows a clear peak at 1.03 GHz with a maximum signal-to-noise ratio (SNR) of 47 dBe, measured across a 100-Hz bandwidth. The bandwidth and SNR of the converted signal are limited by the conversion efficiency, which in turn is limited by the phase mismatch.

## IV. Phase-Matching Considerations

Wavelength conversion in silicon waveguides using the Raman susceptibility requires phase matching between Stokes, anti-Stokes, and pump waves, which span $\sim$200 nm in wavelength. Such widely spaced channels make phase matching a

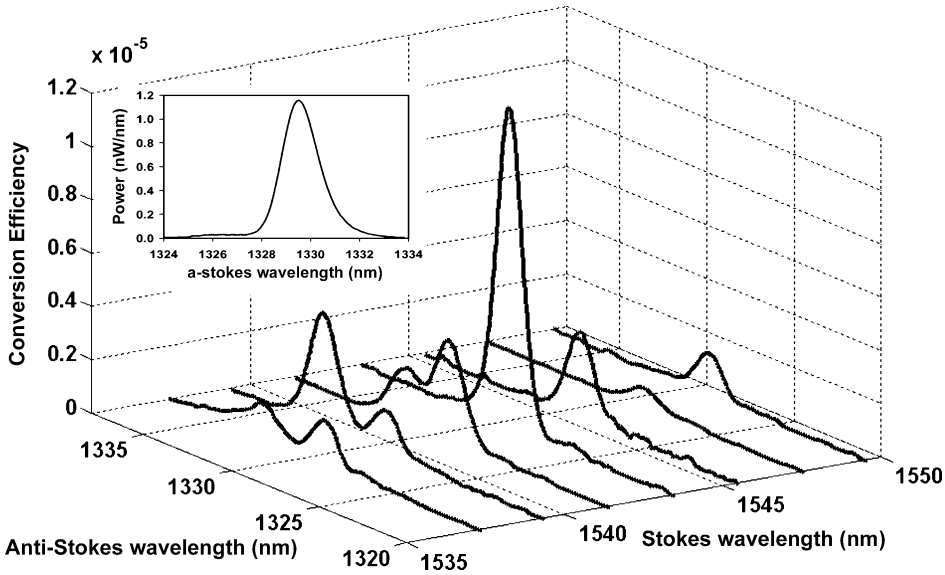


Fig. 10. Variation of Stokes-to-anti-Stokes conversion efficiency as obtained using the optical spectrum analyzer for Stokes wavelength detuning from 1535 to 1550 nm. Clear peak is obtained corresponding to the Raman resonance peak. The secondary peaks are due to the $\mathrm{Sinc}^2$ dependence of efficiency on $\Delta k$. The inset shows the anti-Stokes-converted power for a pump power of 0.23 W and signal power of 1.8 mW. A maximum conversion efficiency of $1.7 \times 10^{-5}$ is obtained using this data.

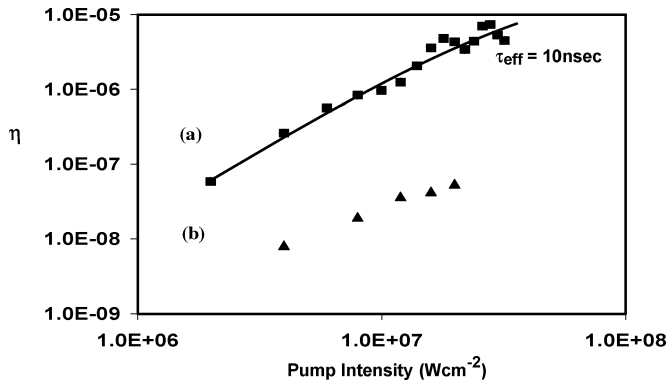


Fig. 11. Experimental plot of conversion efficiency versus pump intensity: (a) both pump and signal are TE polarized (no birefringence). Theoretical fit shows good agreement for effective lifetimes $\tau_{\text{eff}} = 10$ ns. (b) Pump and signal are TE- and transverse-magnetic (TM)-polarized, respectively (with birefringence). With birefringence, the conversion is found to be less efficient.

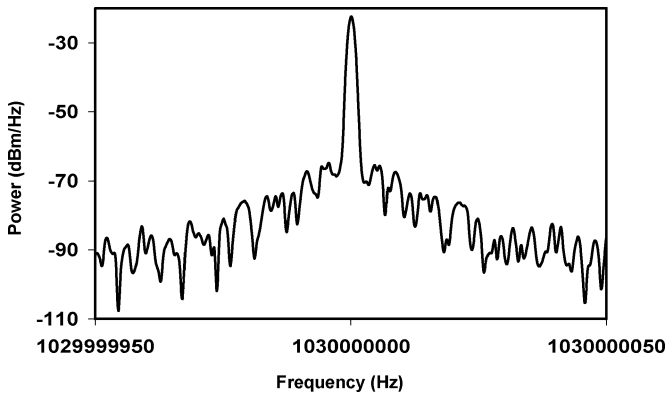


Fig. 12. Conversion of analog RF signal (centered at 1.03 GHz) from Stokes to anti-Stokes. Electrical SNR of 47 dBe was obtained over a bandwidth of 100 Hz.

necessary condition for high-efficiency conversion. Phase mismatch, and hence dispersion, in the waveguides are determined by the waveguide structure and its dimensions.

The phase mismatch between the pump, Stokes, and anti-Stokes waves can be expanded in terms of its various contributions as

$$\begin{aligned}\Delta k &= 2k_P^i - k_S^j - k_A^j \\ &= 2\left(k_P^i - k_P^j\right) - \left.\frac{\partial^2 k}{\partial \omega^2}\right|_{\text{wg}}^{j} \Omega^2 - \left.\frac{\partial^2 k}{\partial \omega^2}\right|_{\text{mat}} \Omega^2 \\ &\quad + \Delta k|_{\substack{\text{SPM} \\ \text{XPM}}} + \Delta k|_{\text{FCR}}. \end{aligned} \tag{5}$$

Here, superscripts $i$ and $j$ refer to the TE or transverse-magnetic (TM) polarizations. The right-hand side of the equation includes the effects of birefringence, material dispersion, waveguide dispersion, and phase mismatch due to self-/cross-phase modulation, and free-carrier refraction, respectively. Here, it is assumed that only the fundamental modes interact in the conversion process. In multimode waveguides, higher order modes can contribute to conversion, making the analysis more complicated. The self- and cross-phase-modulation phase mismatches have been calculated to be approximately $-0.2$ cm$^{-1}$ at typical CW pump powers coupled into the waveguide [22]. Hence, the phase mismatch due to these effects is negligible when compared with the other dispersion contributions as explained subsequently.

The TPA-induced free carriers also lead to a change in refractive index due to free-carrier refraction effects. This can be calculated based on the Drude model as [25]

$$\begin{aligned}\Delta n &= -\frac{e^2\lambda^2}{8\pi^2 c^2 \varepsilon_o n} \cdot \left(\frac{\Delta N_e}{m_{\text{ce}}^*} + \frac{\Delta N_h}{m_{\text{ch}}^*}\right) \\ &\approx 2.87 \times 10^{-21} \cdot \frac{\lambda(\mu\text{m})^2}{n} \cdot \frac{\beta I_p^2 \tau_{\text{eff}}}{2E_p}. \end{aligned} \tag{6}$$

At carrier concentration $\Delta N = 10^{17}$ cm$^{-3}$, which is achieved at a pump intensity of $7 \times 10^7$ W/cm$^2$ and $\tau_{\text{eff}} \sim 10$ ns,

TABLE I
MODAL INDEX AT PUMP, STOKES, AND ANTI-STOKES WAVELENGTHS ALONG WITH THE PHASE MISMATCH DUE TO FREE-CARRIER REFRACTION. DIFFERENT POLARIZATION CONFIGURATIONS ARE ALSO CONSIDERED

| $\lambda$ | $n^{TE}$ | $n^{TM}$ |
|---|---|---|
| 1328.8nm | 3.427 | 3.400 |
| 1427.3nm | 3.406 | 3.379 |
| 1542.3nm | 3.384 | 3.360 |
| $\Delta k_{FCR}(cm^{-1})$ | $\Delta k^{TE-TE}$ = -0.063<br>$\Delta k^{TE-TM}$ =-0.137 | $\Delta k^{TM-TM}$ = -0.058<br>$\Delta k^{TM-TE}$ = +0.015 |

the contribution of free-carrier refraction to phase mismatch can be written as

$$\Delta k_{\mathrm{FCR}} \approx 2\pi \cdot 1.86 \times 10^{8} \cdot \left( \frac{2\lambda_P}{n_P} - \frac{\lambda_S}{n_S} - \frac{\lambda_A}{n_A} \right). \quad (7)$$

Table I lists the free-carrier refraction phase mismatch for various polarization configurations. The effective modal index was calculated for the waveguide structure using BPM simulations. Here, TE–TE and TM–TM refers to pump, Stokes, and anti-Stokes waves having same polarization, and TE–TM and TM–TE refers to a cross-polarized configuration of pump and Stokes/anti-Stokes waves. The phase mismatch due to free-carrier refraction is negligible at the pump intensities achieved under CW pumping. Hence, we can conclude that the presence of free carriers does not materially change the phase-matching criterion.

The material dispersion of silicon follows the Sellemier equation and, being in the normal dispersion regime, the contribution to phase mismatch is on the order of $-110\ \mathrm{cm}^{-1}$ at the pump wavelength used in our experiments. This is significant and has to be compensated by the combined contributions of birefringence and waveguide dispersion effects [22].

The change in the relative contributions of birefringence and waveguide dispersion as the waveguide dimensions are scaled to submicrometer sizes are studied hereafter based on BPM simulation (see Fig. 13). In these simulations, the rib-waveguide dimensions are taken as $w = H$ and $h = 0.6H$. In waveguides with micrometer-sized dimensions, waveguide dispersion is close to $10\ \mathrm{cm}^{-1}$, and birefringence can be made close to $+100\ \mathrm{cm}^{-1}$ by choosing appropriate rib-waveguide dimensions in order to cancel material dispersion [22]. As the waveguide dimensions are scaled down to submicrometer regimes, both birefringence and waveguide dispersion increase. Birefringence increases dramatically [Fig. 13(a)] to the extent that it overcompensates the material dispersion. Similar dispersion curves have been obtained for dense-wavelength-division-multiplexed (DWDM) components [31]. Fortunately, waveguide dispersion also increases [Fig. 13(b)] sufficiently such that it can provide efficient conversion without the contribution of birefringence. This is clearly observed in the experimental results of Fig. 11, where without birefringence, high conversion efficiency is achieved, whereas with birefringence, the efficiency is significantly lower.

As the rib dimensions are reduced further, waveguide dispersion is found to reach a maximum positive value and then reduce

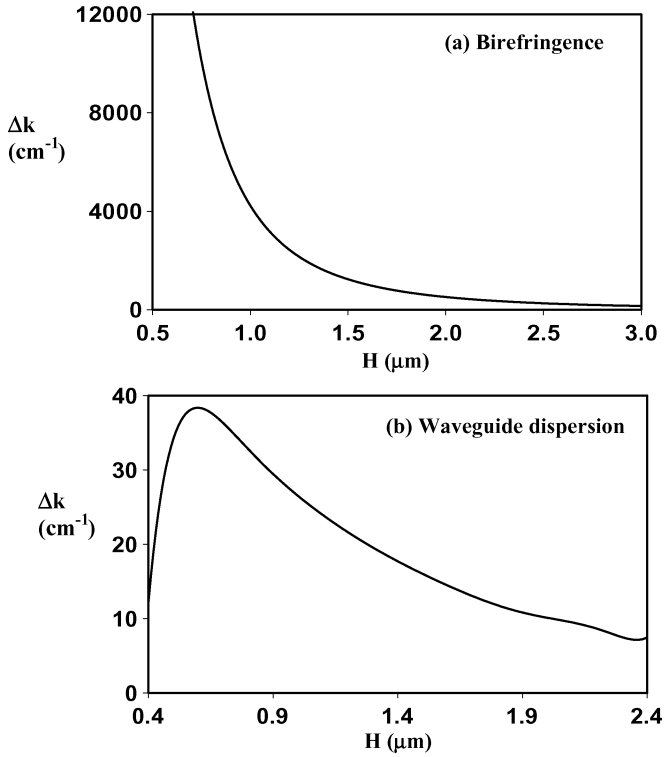


Fig. 13. Variation of (a) birefringence and (b) waveguide dispersion as the rib-waveguide dimensions are scaled down. The scaling is done with $H = w$ and slab height $h = 0.6H$. Both birefringence and waveguide dispersion increases with reduction in dimensions. Birefringence increases dramatically such that it overcompensates for material dispersion ($\sim -110\ \mathrm{cm}^{-1}$). Waveguide dispersion also increases and can be used to partially cancel out material dispersion without the contribution of birefringence.

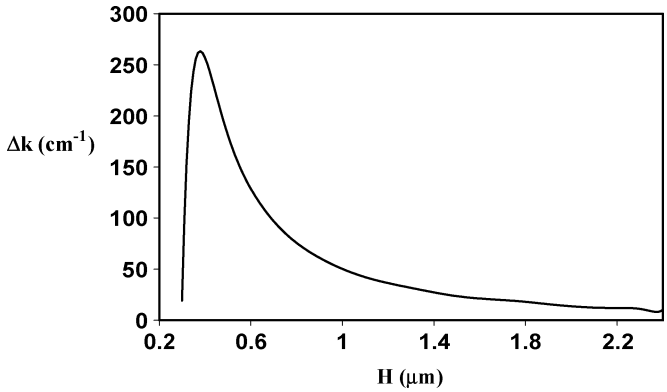


Fig. 14. Variation of waveguide dispersion as the channel waveguide dimensions are scaled down. The scaling is done with $H = w$. Waveguide dispersion increases substantially that it can be used to compensate material dispersion of $-110\ \mathrm{cm}^{-1}$ completely and provide phase matching.

and eventually become negative [32]. This would result in partial compensation of material dispersion and limit the minimum achievable phase mismatch. However, waveguide dispersion increases substantially as the slab region is etched and the waveguide approaches channel geometry. The variation of waveguide dispersion in a channel waveguide as the dimensions are scaled down is shown in Fig. 14. Similar dispersion curves have been obtained for silicon wire waveguides [32]. Considering only fundamental modes to interact, channel waveguides of dimensions $\sim 0.7\ \mu\mathrm{m} \times 0.7\ \mu\mathrm{m}$ and $\sim 0.3\ \mu\mathrm{m} \times 0.3\ \mu\mathrm{m}$ attain enough

waveguide dispersion to completely cancel out material dispersion and hence achieve phase matching. However, the slope of the $\Delta k$ versus $H$ curve in Fig. 14 suggests that for $H < 0.4\ \mu$m, waveguide dispersion is extremely sensitive to height variations, making it difficult to control the dimensions in order to achieve phase matching.

## V. Conclusion

Parametric Raman nonlinearities and its application in realizing wavelength conversion are studied theoretically and experimentally in submicrometer-modal-area silicon waveguides. The combined effects of Raman nonlinearities and free-carrier losses induced by two-photon absorption (TPA) nonlinearities have been analyzed using the coupled-mode equations. It is found that reducing carrier lifetime close to 1 ns would reduce free-carrier effects to negligible levels. Scaling down the waveguide dimensions to submicrometer regimes would help in enhancing the Raman nonlinearities and reducing the free-carrier lifetime. High optical intensity also relieves the stringent requirements on phase mismatch to achieve high conversion efficiency. Experimentally, a conversion efficiency of $1.7 \times 10^{-5}$ has been obtained. The figure of merit of the conversion process, which is defined as the ratio of the conversion efficiency to the effective pump power in these waveguides, is found to be more than five times larger than the authors' previous report on micrometer-sized waveguides. This improvement can be attributed to the increased Raman nonlinearities and reduced carrier lifetime. The feasibility of this scheme toward data conversion has also been demonstrated. The dispersion properties of these waveguides are found to be different from the authors' previous work on micrometer-sized waveguides. In the submicrometer regime, the waveguide dispersion increases so significantly that it can help in partially compensating material dispersion and achieve efficient conversion. It is also found that submicrometer channel waveguides can help achieving complete phase matching and, hence, enhance the conversion efficiency by several orders of magnitude.

## Acknowledgment

The authors would like to thank Dr. J. Shah for his support.

## References

[1] G. T. Reed, "Optical age of silicon," *Nature*, vol. 427, pp. 595–596, 2004.
[2] B. Jalali, S. Yegnanarayanan, T. Yoon, T. Yoshimoto, I. Rendina, and F. Coppinger, "Advances in silicon-on-insulator optoelectronics," *IEEE J. Sel. Topics Quantum Electron.*, vol. 4, no. 6, pp. 938–947, Nov.–Dec. 1998.
[3] L. Pavesi, L. D. Negro, G. Mazzoleni, G. Franzo, and S. Priolo, "Optical gain in silicon nanocrystals," *Nature*, vol. 408, pp. 440–444, 2000.
[4] S. Saini *et al.*, "High index contrast silicon oxynitride materials platform for Er-doped microphotonic amplifiers," presented at the Material Research Society (MRS) Spring Meeting, San Francisco, CA, Apr. 12–16, 2004.
[5] A. Polman and F. C. J. M. Van Veggel, "Broadband sensitizers for erbium-doped planar optical amplifiers: review," *J. Opt. Soc. Amer. B, Opt. Phys.*, vol. 21, pp. 871–892, 2004.
[6] J. Lee, J. Shin, and N. Park, "Optical gain in Si-nanocrystal sensitized, Er-doped silica waveguide using top-pumping 470 nm LED," presented at the Optical Fiber Communication Conf., Los Angeles, CA, Feb. 22–27, 2004, Postdeadline Paper.
[7] J. Ruan, P. M. Fauchet, L. D. Negro, M. Cazzanelli, and L. Pavesi, "Stimulated emission in nanocrystalline silicon superlattices," *Appl. Phys. Lett.*, vol. 83, pp. 5479–5481, 2003.
[8] A. Liu *et al.*, "A high-speed silicon optical modulator based on a metal-oxide-semiconductor capacitor," *Nature*, vol. 427, pp. 615–618, 2004.
[9] C. A. Barrios, V. R. Almeida, R. Panepucci, and M. Lipson, "Electrooptic modulation of silicon-on-insulator submicrometer size waveguide devices," *J. Lightw. Technol.*, vol. 21, no. 10, pp. 2332–2339, Oct. 2003.
[10] J. Oh, S. K. Banerjee, and J. C. Campbell, "Metal-germanium-metal photodetectors on heteroepitaxial Ge-on-Si with amorphous Ge Schottky barrier enhancement layers," *IEEE Photon. Technol. Lett.*, vol. 16, no. 2, pp. 581–583, Feb. 2004.
[11] R. Claps, D. Dimitropoulos, V. Raghunathan, Y. Han, and B. Jalali, "Observation of stimulated Raman scattering in silicon waveguides," *Opt. Express*, vol. 11, pp. 1731–1739, 2003.
[12] T. K. Liang and H. K. Tsang, "Role of free carriers from two-photon absorption in Raman amplification in silicon-on-insulator waveguide structures," *Appl. Phys. Lett.*, vol. 84, pp. 2745–2747, 2004.
[13] R. L. Espinola, J. I. Dadap, R. M. Osgood Jr., S. J. McNab, and Y. A. Vlasov, "Raman amplification in ultrasmall silicon-on-insulator wire waveguides," *Opt. Express*, vol. 12, pp. 3713–3718, 2004.
[14] T. K. Liang and H. K. Tsang, "Pulsed-pumped silicon-on-insulator waveguide Raman amplifier," , Hong Kong, Sep. 29–Oct. 4, 2004, Paper WA4.
[15] A. Liu, H. Rong, M. Paniccia, O. Cohen, and D. Hak, "Net optical gain in a low loss silicon-on-insulator waveguide by stimulated Raman scattering," *Opt. Express*, vol. 12, pp. 4261–4268, 2004.
[16] R. Claps, V. Raghunathan, D. Dimitropoulos, and B. Jalali, "Anti-stokes Raman conversion in silicon waveguides," *Opt. Express*, vol. 11, pp. 2862–2872, 2003.
[17] V. Raghunathan, R. Claps, D. Dimitroupoulos, and B. Jalali, "Wavelength conversion in silicon using Raman induced four-wave mixing," *Appl. Phys. Lett.*, vol. 84, pp. 34–36, 2004.
[18] O. Boyraz, T. Indukuri, and B. Jalali, "Self-phase-modulation induced spectral broadening in silicon waveguides," *Opt. Express*, vol. 12, pp. 829–834, 2004.
[19] O. Boyraz, P. Koonath, V. Raghunathan, and B. Jalali, "All optical switching and continuum generation in silicon waveguides," *Opt. Express*, vol. 12, pp. 4094–4102, 2004.
[20] T. K. Liang *et al.*, "Silicon waveguide two-photon absorption detector at 1.5 $\mu$m wavelength for autocorrelation measurements," *Appl. Phy. Lett.*, vol. 81, pp. 1323–1325, 2002.
[21] H. Fukuda *et al.*, *Silicon Wire Waveguides and Their Application for Microphotonics Devices*. San Francisco, CA: Integrated Photonic Research Conf., Jun. 30–Jul. 2, 2004.
[22] D. Dimitropoulos, V. Raghunathan, and R. Claps, "Phase-matching and nonlinear optical processes in silicon waveguides," *Opt. Express*, vol. 12, pp. 149–160, 2004.
[23] J. J. Wynne, "Optical third-order mixing in GaAs, Ge, Si, and InAs," *Phys. Rev.*, vol. 178, pp. 1295–1303, 1969.
[24] K. W. Delong and G. I. Stegeman, "Two-photon absorption as a limitation to all-optical waveguide switching in semiconductors," *Appl. Phys. Lett.*, vol. 57, pp. 2063–2064, 1990.
[25] R. A. Soref and B. R. Bennett, "Electrooptical effects in silicon," *IEEE J. Quantum Electron.*, vol. QE-23, no. 1, pp. 123–129, Jan. 1987.
[26] M. A. Mendicino, Comparison of properties of available SOI materials, in Properties of Crystalline Silicon, pp. 992–1001, 1998.
[27] D. Dimitropoulos, R. Jhaveri, R. Claps, J. C. S. Woo, and B. Jalali, "Lifetime of photo-generated carriers in silicon-on-insulator rib waveguides," *Appl. Phys. Lett.*, vol. 86, p. 71 115, 2005.
[28] E. Golovchenko, P. V. Mamyshev, A. N. Pilipetskii, and E. M. Dianov, "Mutual influence of the parametric effects and stimulated Raman scattering in optical fibers," *IEEE J. Quantum Electron.*, vol. 26, no. 10, pp. 1815–1820, Oct. 1990.
[29] D. Dimitropoulos, R. Claps, Y. Han, and B. Jalali, "Nonlinear optics in silicon waveguides: Stimulated Raman scattering and two-photon absorption," in *Proc. SPIE*, vol. 4987, 2003, pp. 140–148.
[30] G. P. Agrawal, *Nonlinear Fiber Optics*, 3rd ed. San Diego, CA: Academic, 2001.
[31] R. J. Bozeat, S. Day, F. Hopper, F. P. Payne, S. W. Roberts, and M. Asghari, "Silicon based waveguides," in *Silicon Photonics*, L. Pavesi and D. J. Lockwood, Eds. New York: Springer-Verlag, 2004, p. 276.
[32] L. Tong, J. Lau, and E. Mazur, "Single-mode guiding properties of subwavelength diameter silica and silicon wire waveguides," *Opt. Express*, vol. 12, pp. 1025–1035, 2004.

**Varun Raghunathan** received the B.E. degree in electrical and electronics engineering from the Birla Institute of Technology and Science, Pilani, India, in 2002 and the M.S. degree in electrical engineering from the University of California, Los Angeles (UCLA), in 2005. He is currently working toward the Ph.D. degree at UCLA.

His research work includes the experimental study of stimulated Raman amplification, wavelength conversion using parametric Raman conversion processes, and fabrication issues of silicon photonic structures. His other research interests include silicon photonics, nonlinear optics, solid-state physics, and quantum electronics.

Mr. Raghunathan was awarded a fellowship by the California Nanosystems Institute (CNSI) for his Master's degree studies.

**Ricardo Claps** received the B.S. degree from the National University of Mexico (UNAM), Mexico City, in 1993 and the Ph.D. degree from the University of Texas, Austin, in 2000. During his doctoral research, he developed a laser-diode-based Raman spectrometer and adapted the system to measure Raman spectra in gas flows. Using that configuration, he also discovered a non-Boltzmann distribution of rotational states in hot $CO_2$ gas flows.

While a Postdoctoral Researcher at Rice University, Houston, TX, he designed and built an ammonia sensor that achieved record sensitivity at the time and was tested in a bioreactor at NASA's Johnson Space Center. As a Postdoctoral Researcher at the University of California, Los Angeles (UCLA), he demonstrated for the first time stimulated Raman amplification and coherent anti-Stokes Raman scattering in silicon waveguides. He is currently pursuing new applications for optics and spectroscopic techniques in medical sciences at Neptec Optical Solutions, Inc., Jefferson City, TN.

**Dimitrios Dimitropoulos** received the B.S. degree in electrical engineering from the National Technical University of Athens, Athens, Greece, in 2000, and the M.S. degree in electrical engineering degree from the University of California, Los Angeles (UCLA), in 2003. He is currently working toward the Ph.D. degree in electrical engineering at UCLA.

His current research is in silicon integrated optical devices, particularly silicon Raman lasers, amplifiers, and wavelength converters. His research interests include areas of quantum electronics and photonics, noise in physical systems and information theory, and solid-state and plasma physics.

**Bahram Jalali** (S'86–M'89–SM'97–F'04) received the B.S. degree in physics from Florida State University, Tallahassee, in 1984 and the M.S. and Ph.D. degrees in applied physics from Columbia University, New York, in 1986 and 1989, respectively.

He was a Member of the Technical Staff at the Physics Research Division of AT&T Bell Laboratories, Murray Hill, NJ, from 1988 to 1993. He joined the Electrical Engineering (EE) Department of the University of California, Los Angeles (UCLA), in 1993, where he is now a full Professor. He is the Chair of the Optoelectronic Circuits and Systems Laboratory, Director of the Defense Advanced Research Projects Agency (DARPA) Consortium for Optical A/D System Technology, and former Chair of the Photonic and Optoelectronics Field of Study in the EE Department. He is the Founder of Cognet Microsystems, Los Angeles, CA, a fiber-optic component company that was acquired by Intel Corporation in April 2001. He is also involved in the new Biomedical Engineering Interdepartmental Program. He has more than 100 publications and holds six patents. His research interests are in radio-frequency photonics, integrated optics, optical communication, and biomedical sensors.

Dr. Jalali has received the BridgeGate 20 Award for his contribution to the Southern California Economy. He was a Distinguished Lecturer of the Orlando Chapter of the IEEE Lasers & Electro-Optics Society (LEOS) in 1998. He was General Chair of the International Microwave Photonics Conference (MWP) in 2001, and he served on the Technical Program Committees for the Conference on Lasers and Electro-Optics (CLEO) and the Integrated Photonic Research (IPR) conference.